

This work was written as part of one of the author's official duties as an Employee of the United States Government and is therefore a work of the United States Government. In accordance with 17 U.S.C. 105, no copyright protection is available for such works under U.S. Law.

Public Domain Mark 1.0

<https://creativecommons.org/publicdomain/mark/1.0/>

Access to this work was provided by the University of Maryland, Baltimore County (UMBC) ScholarWorks@UMBC digital repository on the Maryland Shared Open Access (MD-SOAR) platform.

Please provide feedback

Please support the ScholarWorks@UMBC repository by emailing scholarworks-group@umbc.edu and telling us what having access to this work means to you and why it's important to you. Thank you.

RESEARCH ARTICLE

10.1002/2013JD020884

Key Points:

- New capabilities in retrieving trace gases by airborne Sun photometry
- Demonstrating ability to measure and track elevated pollution layers
- Using measured and retrieved data products to cluster pollution sources

Correspondence to:

M. Segal-Rosenheimer,
michal.segalrosenhaimer@nasa.gov

Citation:

Segal-Rosenheimer, M., et al. (2014), Tracking elevated pollution layers with a newly developed hyperspectral Sun/Sky spectrometer (4STAR): Results from the TCAP 2012 and 2013 campaigns, *J. Geophys. Res. Atmos.*, 119, 2611–2628, doi:10.1002/2013JD020884.

Received 12 SEP 2013

Accepted 29 JAN 2014

Accepted article online 4 FEB 2014

Published online 5 MAR 2014

Tracking elevated pollution layers with a newly developed hyperspectral Sun/Sky spectrometer (4STAR): Results from the TCAP 2012 and 2013 campaigns

M. Segal-Rosenheimer^{1,2}, P. B. Russell¹, B. Schmid³, J. Redemann¹, J. M. Livingston⁴, C. J. Flynn³, R. R. Johnson¹, S. E. Dunagan¹, Y. Shinozuka^{1,2}, J. Herman^{5,6}, A. Cede⁶, N. Abuhassan⁶, J. M. Comstock³, J. M. Hubbe³, A. Zelenyuk³, and J. Wilson³
¹NASA Ames Research Center, Moffett Field, California, USA, ²Bay Area Environmental Research Institute, Sonoma, California, USA, ³Pacific Northwest National Laboratory, Richland, Washington, USA, ⁴SRI International, Menlo Park, California, USA, ⁵JCET - Joint Center for Earth Systems Technology, University of Maryland, Baltimore County, Baltimore, Maryland, USA, ⁶NASA Goddard Space Flight Center, Greenbelt, Maryland, USA

Abstract Total columnar water vapor (CWV), nitrogen dioxide (NO₂), and ozone (O₃) are derived from a newly developed, hyperspectral airborne Sun-sky spectrometer (4STAR) for the first time during the two intensive phases of the Two-Column Aerosol Project (TCAP) in summer 2012 and winter 2013 aboard the DOE G-1 aircraft. We compare results with coincident measurements. We find 0.045 g/cm² (4.2%) negative bias and 0.28 g/cm² (26.3%) root-mean-square difference (RMSD) in water vapor layer comparison with an in situ hygrometer and an overall RMSD of 1.28 g/m³ (38%) water vapor amount in profile by profile comparisons, with differences distributed evenly around zero. RMSD for O₃ columns average to 3%, with a 1% negative bias for 4STAR compared with the Ozone Measuring Instrument along aircraft flight tracks for 14 flights during both TCAP phases. Ground-based comparisons with Pandora spectrometers at the Goddard Space Flight Center, Greenbelt, Maryland, showed excellent agreement between the instruments for both O₃ (1% RMSD and 0.1% bias) and NO₂ (17.5% RMSD and −8% bias). We apply clustering analysis of the retrieved products as a case study during the TCAP summer campaign to identify variations in atmospheric composition of elevated pollution layers and demonstrate that combined total column measurements of trace gas and aerosols can be used to define different pollution layer sources, by comparing our results with trajectory analysis and in situ airborne miniSPAT (single-particle mass spectrometer) measurements. Our analysis represents a first step in linking sparse but intense in situ measurements from suborbital campaigns with total column observations from space.

1. Introduction

The detailed quantification of atmospheric constituents, such as trace gases and aerosols, including their horizontal and vertical distributions in the atmosphere, is important for understanding climate change, radiation budgets, and air pollution. Aerosol surfaces, together with NO₂, water vapor, and O₃, play important roles in many tropospheric chemical reactions [e.g., Finlayson-Pitts and Pitts, 2000]. For example, the reaction of NO₂ and water vapor to form HONO, which is an important step in the tropospheric ozone cycle, has been proven to be accelerated by surfaces such as soot [e.g., Ammann et al., 1998]. In addition, biomass burning (BB) is associated with NO_x emissions that convert to NO₂, both at the initial flaming stage and as a result of oxidation processes of peroxyacetyl-nitrate or other forms of organic oxides of nitrogen. The NO₂ amounts associated with biomass-burning plumes are related to the age of the plume, to fuel type, and to the environmental conditions [Finlayson-Pitts and Pitts, 2000; Yokelson et al., 2009; Burling et al., 2010, 2011]. Moreover, previous airborne observations and modeling analyses have shown that smoke plumes can influence O₃ concentrations, even at very long distances from the initial fire emission locations [Dupont et al., 2012, and references therein]. Hence, the capability to concurrently measure NO₂, O₃, and aerosol properties at high spatial and temporal resolution would be useful not only to identify various polluted air masses but also to characterize differences in chemical composition between fresh and aged pollution.

However, in many ground-based and airborne applications such concurrent measurements are not available. For example, ground-based (e.g., Aerosol Robotic Network (AERONET)) and airborne Sun photometers measure

only aerosol and water vapor using the 940 nm absorption band [e.g., *Livingston et al.*, 2007], and have some limited ability to measure O_3 in very large slant-path cases when aerosol optical depth (AOD) is sufficiently small (i.e., $< \sim 0.03$ at 600 nm [e.g., *Livingston et al.*, 2005]). The ground-based Pandora spectrometer system is a relatively new direct-Sun- and sky-viewing instrument that was developed for trace-gas retrievals, using high-spectral-resolution (0.6 nm) spectrometers, but its aerosol measurement capabilities are limited to the spectral range of 265–530 nm [e.g., *Herman et al.*, 2009]. The newly developed Spectrometer for Sky-Scanning, Sun-Tracking Atmospheric Research (4STAR, [Dunagan et al., 2013]) provides this combination of concurrent trace-gas and aerosol measurements, and in this paper we demonstrate 4STAR's potential to extend our detection and quantification of atmospheric composition from different pollution sources.

In particular, the 4STAR instrument combines the airborne Sun-tracking capabilities of the NASA Ames Airborne Tracking Sunphotometer (AATS-14) [Russell et al., 2005] and an AERONET-like [Holben et al., 2001] sky-scanning capability with state-of-the-art Zeiss spectrometers. One of the unique features of this instrument, stemming from its design using grating spectrometers that cover the UV-VIS-SWIR (Ultra-Violet-Visible-Short-Wave-Infrared) spectral range (i.e., 350–1700 nm), is its capability to measure atmospheric trace gases such as water vapor, O_3 , and NO_2 concurrently with a wide spectral range for aerosol optical depth (AOD), which allows the characterization of various aerosol properties (e.g., extinction Ångström exponent and absorption Ångström exponent) to facilitate their classification. In contrast, both OMI (Ozone Monitoring Instrument) and the Pandora ground-based instruments [Herman et al., 2009] span only UV-VIS spectral region for aerosol measurements (500 nm and 530 nm, respectively). Moreover, the current generation of Sun photometers, for example, the AATS-14 [Russell et al., 2005] and the AERONET Sun-sky photometers [Holben et al., 2001], are optimized to yield the best AOD estimate by selecting discrete, narrow wavelength bands that minimize most absorbing gas contributions and so do not have the simultaneous capability to retrieve O_3/NO_2 amounts (see further discussion below).

These unique features of 4STAR have the potential to improve our knowledge of columnar and profile concentrations of water vapor, O_3 , NO_2 , and aerosol and to answer questions related to air pollution, tropospheric composition, chemistry, and radiation.

Recently, *Shinozuka et al.* [2013] presented and validated the aerosol measurement capability of the 4STAR. Our goal in this paper is to demonstrate the newly developed capability to retrieve total column trace-gas amounts from 4STAR measurements and to test whether the combination of the 4STAR's aerosol and trace-gas products can be used to identify the composition of gas/aerosol upper tropospheric pollution layers that originate from different sources. First we give a brief description of the 4STAR instrument specifications, describe our trace-gas retrieval methods, and present comparisons with ground-based in situ and satellite-borne measurements to evaluate the 4STAR trace-gas products. This is followed by a clustering analysis of different pollution sources for pollution layers observed during the Two-Column Aerosol Project (TCAP) summer phase in 2012. This analysis uses the aerosol and trace-gas products retrieved from 4STAR measurements to test whether they can be used to characterize various polluted air masses. The analysis is supported by observations of the HSRL-2 (High Spectral Resolution Lidar-2) aboard the B-200 aircraft and by specific composition analysis by the miniSPLAT (single-particle mass spectrometer) aboard the G-1 aircraft.

2. Instruments, Retrieval Procedures, and Measurements

2.1. 4STAR

The 4STAR instrument operates in three different modes: Sun-tracking, sky-scanning, and zenith pointing. Here we focus on the trace-gas retrieval capability from the direct-Sun-tracking mode. Other Sun-tracking mode capabilities such as AOD and cirrus optical properties can be found in *Shinozuka et al.* [2013] and in *Segal-Rosenheimer et al.* [2013], respectively. A detailed description of the instrument technical features, airworthiness tests, and certification can be found in *Dunagan et al.* [2013].

In brief, the instrument has two structurally rigid grating array spectrometers that cover the UV-SWIR (UV-VIS-NIR, 210–995 nm: Tec5 MCS charge-coupled device (CCD) with a 1044-channel Hamamatsu S7031-1006 CCD detector, hereafter UVNIR spectrometer; and SWIR, 950–1703 nm: Tec5 NIR-PGS 1.7 with a 512-channel Sensors Unlimited Inc. Multiplexed InGaAs SU 512LD-1.7 T1 diode array, hereafter

SWIR spectrometer) that are combined to yield continuous spectra. The sampling rate is 1 Hz, and the nominal integration times are 50 (with six spectra averaged per one sampling period) and 400 ms (one spectrum per one sampling period) for the UVNIR and SWIR spectrometers, respectively. The sampling period is longer than the integration times because it refers to the overall acquisition time, including instrument delay time and control loops. The integration time of each spectrometer can be adjusted during flight according to the relevant atmospheric conditions and observation modes. The nominal integration times used in TCAP were proven to be robust in many atmospheric conditions during the many data acquisition tests performed at NASA Ames with 4STAR.

The 4STAR light collection system has fiber optic bundle foreoptics that is connected to the spectrometers. A two-axis motion control system with analog feedback control provides active tracking of the solar disk. The instrument full field of view (FOV) is $\sim 1.25^\circ$. While tracking the Sun, active alignment to the solar disk relies on the differential analog signal provided by a quadrant photodiode detector coaligned with the Sun collector. A deviation from the FOV plateau center may cause signal deterioration and wavelength-dependent effects; hence, data with tracking errors $> 0.25^\circ$ (determined by measuring voltage differences between two opposite sides of the Sun quadrant detector and converting them to the location on the FOV plateau based on FOV reference measurements) are excluded from the data used for the retrieval (see also Dunagan *et al.* [2013] and Shinozuka *et al.* [2013] for a more detailed description).

During data acquisition, dark counts are measured every 20 min with a shutter mechanism and accounted for in the analyses of the data. The data shown in this manuscript are based only on UVNIR spectrometer measurements. This spectrometer has a nearly symmetric Gaussian point spread function (PSF), a wavelength-dependent FWHM (full width at half maximum) resolution of 2–3 nm in the spectral range used for the O_3 and NO_2 (430–675 nm) retrievals, and FWHM resolution of 4–7 nm in the spectral range used for the water vapor retrieval (940–960 nm), with spectral sampling of 2–3 for FWHM.

The instrument spectral resolution and calibration is characterized by measuring a series of sharp emission line lamps (i.e., HgAr, Kr, Ne, Xe, and Cd). Comparing theoretical line positions to the measured ones yields an improved wavelength registration and wavelength-dependent FWHM values. This procedure follows the one developed for the Pandora instrument [Cede, 2012] and was carried out in the NASA Goddard calibration lab in March 2013 during an intercomparison measurement and calibration campaign with 4STAR and Pandora instruments.

The instrument transmittance is derived by dividing the measured digital count rate C (dark subtracted and normalized by integration time) by the instrument reference spectrum, C_0 , and by the corresponding Earth-Sun distance correction. C_0 is determined by the refined Langley extrapolation method [e.g., Schmid and Wehrli, 1995], which measures the instrument output over a large air mass range to extrapolate to zero air mass top-of-atmosphere (TOA) instrument PSF-weighted solar spectrum (hereafter C_0). This is done in spectral regions that follow the Beer-Lambert extinction law at 4STAR's wavelength resolution (including the O_3 and NO_2 spectral regions used in the present analysis). During the TCAP campaign, this calibration was done in-flight (hereafter an airborne Langley calibration) at constant altitudes of 6 km and 6.85 km for the summer (22 July 2012) and winter (12 and 14 February 2013) phases, respectively. The advantage of such a calibration is that it accesses pristine atmospheric conditions, with minimal interference from tropospheric aerosols and gases, in a short amount of time with the instrument remaining in the operational configuration employed for the regular research flights. A detailed description of the 4STAR C_0 derivation and its uncertainty is given in Shinozuka *et al.* [2013], Appendix A.

For the ensuing trace-gas retrieval, we applied the following two filtering criteria to reduce data contaminated by clouds and instrument tracking errors: (1) a standard deviation of count rate at the 670 nm nonabsorbing region that is smaller than 1% of the average measured signal during a 3 s measurement period, which represents noisy data rather than gas absorption variations, and (2) a tracking error of less than 0.25° .

2.2. 4STAR Trace-Gas Retrievals

This section summarizes the retrievals from the direct-Sun mode of 4STAR. In short, we describe here the columnar water vapor retrievals that follow the well-established heritage scheme of AATS-14 [e.g., Livingston *et al.*, 2007], using a modified Langley technique [e.g., Schmid *et al.*, 1996], modified to the 4STAR

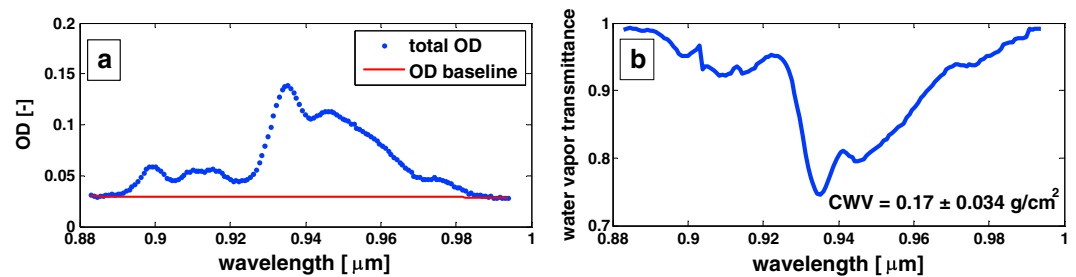


Figure 1. Measured spectra of (a) AOD amount deduced by a linear baseline fit (solid red line) to the water vapor region at 940 nm (blue dots), as detailed in text, and (b) water vapor in the 940 nm spectral region, as derived by applying the modified Langley method, as detailed in text. The corresponding CWV amount is shown in the insert.

hyperspectral characteristics, and the O_3/NO_2 retrievals that follow a linear least squares fit retrieval over the spectral ranges of 430–490 nm and 490–675 nm for NO_2 and O_3 , respectively. Our O_3/NO_2 retrieval approach includes some modifications to the classic differential optical absorption spectroscopy (DOAS) retrieval method, due to the broader spectral range and lower resolution of 4STAR relative to other DOAS instruments. Specifically, we are utilizing the full spectral range in our Rayleigh subtracted optical depth (OD) before retrieving O_3/NO_2 and additionally utilize the 490–870 nm spectral region to construct an aerosol baseline in our O_3 retrieval procedure.

2.2.1. Columnar Water Vapor

The derivation of columnar water vapor (CWV) is based on AATS-14 water vapor retrieval heritage that uses the strong water vapor absorption band at 940 nm [Schmid *et al.*, 1996, 2001; Ingold *et al.*, 2000; Livingston *et al.*, 2007]. In short, the water vapor amount is derived by inverting the measured transmittance, using the following water vapor band parameterization, which is a function of columnar water vapor and air mass (adopted from Ingold *et al.* [2000]):

$$T_w(\lambda) = c * \exp(-a(\lambda)(WVs)^{b(\lambda)}) \quad (1)$$

where T_w is the water vapor transmittance, and a , b , and c are wavelength λ dependent coefficients derived from a least squares fitting of water vapor transmittances for various model atmospheres (midlatitude summer and midlatitude winter for the corresponding TCAP phases, respectively) and altitudes over a range of slant water vapor amount (see Livingston *et al.* [2007] for detailed description of the coefficient derivation). In this analysis we set the c parameter to unity. Transmittance calculations are performed using the line-by-line radiative transfer code LBLRTM V9.2 [Clough *et al.*, 2005], and WVs is the slant water vapor path, which is the product of water vapor air mass (m_w) and CWV.

In the case of water vapor, which is a strong absorber that does not follow the Beer-Lambert law, the standard C_0 calibration does not hold at 4STAR's wavelength resolution, and a modified calibration coefficient (hereafter C_{OM}) is derived. The modification from the standard Langley method is that the aerosol optical depth (AOD) has to be deduced and subtracted in the water vapor region before the Langley extrapolation is made [e.g., Schmid *et al.*, 1996]. To do that, we calculate the aerosol contribution in the water vapor spectral region by fitting a linear (in $\log(\lambda)$ - $\log(OD)$ coordinates) baseline between 880 and 990 nm (see solid red line in Figure 1a) region. Figure 1b shows the measured water vapor band transmittance, derived by applying the modified Langley method.

By inverting the measured transmittance (calculated using C_{OM}), given the air mass and spectral coefficients, we extract the CWV amount at each of the water vapor wavelengths. The resulting value is averaged over the 940–960 nm spectral range, which covers the maximal absorption region and shows a minimal wavelength dependency of the CWV amounts derived from the LBLRTM procedure (not shown). The total uncertainty is calculated as a root-mean-square of C_{OM} uncertainty and the spectral standard deviation variation (over the 940–960 nm spectral range) for each of the data points. The C_{OM} uncertainty was assumed to span the range of C_{OM} values calculated using either a two-parameter fit (as described here) or as three-parameter fit (as described in Ingold *et al.* [2000]) for the corresponding altitudes during the Langley flights, and it is 2.5%.

2.2.2. NO₂ and O₃

O₃ and NO₂ retrievals are based on a spectral least squares linear fit to the total slant path optical depth (OD) after subtraction of the Rayleigh scattering OD wavelength-dependent component. We start with the total slant path optical depth (including Rayleigh), which is defined as follows:

$$OD_t(\lambda) = -\text{LOG}(C/C_0) = m_R \tau_R(\lambda) + m_a \tau_a(\lambda) + m_{O_3} \tau_{O_3}(\lambda) + m_{NO_2} \tau_{NO_2}(\lambda) + m_{H_2O} \tau_{H_2O}(\lambda) + m_{O_4} \tau_{O_4}(\lambda) \quad (2)$$

where m and τ correspond to the specific component air mass factor and optical depth, respectively, and subscripts R, a, O₃, NO₂, H₂O, and O₄ correspond to atmospheric molecular scattering (Rayleigh), aerosol extinction, ozone, nitrogen dioxide, water vapor, and oxygen dimer (O₂-O₂) absorption components, which are the strongest absorption gases in the spectral region of the retrieval. The Rayleigh OD is the product of the atmospheric molecular scattering τ_R , which is calculated after *Bucholtz* [1995], and the molecular scattering air mass factor, which is calculated after *Kasten and Young* [1989]. Static atmospheric pressure needed for the calculation is taken from the aircraft telemetry data file. O₃ and NO₂ air mass factors are calculated after *Komhyr* [1980], with effective heights of peak amounts of O₃ and NO₂ taken at altitudes of 21 and 25 km, respectively. The water vapor air mass factor is calculated after *Kasten* [1965].

C_0 is the 4STAR wavelength-dependent calibration coefficient, as described earlier in text. In the derivation of C_0 , O₃ and NO₂ column amounts and air mass values have to be taken into account (see *Schmid and Wehrli* [1995], equations 1–7, for details). In our analysis, the former are taken from the corresponding OMI O₃ (level-2 OMTO3 product [*Bhartia*, 2002]) amount above the instrument/aircraft and from the stratospheric NO₂ (level-2 OMNO2 product [*Boersma et al.*, 2002]) products measured at the time of the airborne Langley calibration, where the latter are calculated as explained above. This approach of deducing a “baseline” amount of O₃ and NO₂ in the measured calibration spectrum is comparable to the Pandora NO₂ and O₃ reference amount derivation [*Herman et al.*, 2009], where the amount of NO₂ in their reference spectrum used as the baseline for retrievals is derived by performing a minimum Langley extrapolation technique over a long measurement period (several weeks) to deduce the NO₂ amounts in the reference spectrum.

It should be noted that to estimate the correct O₃ amount above the instrument we must scale the total OMI column to match the aircraft/instrument altitude. To do that, we calculate fifth-order polynomials that fit the cumulative sum of the climatological O₃ profiles versus z^* altitude (as in *McPeters and Labow* [2012]) in km ($z^* = 16 \cdot \text{LOG}_{10}[1013/P]$, where P is pressure in hPa) for the latitude belt of 30–40°N during July and February (corresponding to the TCAP summer and winter phases, respectively). We use the new O₃ climatology database by *McPeters and Labow* [2012], which includes Microwave Limb Sounder data from 2004 to 2010 and sonde data from 1998 to 2010. To scale 4STAR retrieved values (OMI total column) we evaluate the polynomial at the corresponding z^* and divide (multiply) this fractional value with the derived 4STAR O₃ (OMI O₃).

For both O₃ and NO₂ retrieval procedures we subtract the OD due to the Rayleigh component (Figure 2a shows an example of Rayleigh subtracted OD) prior to the retrieval inversion. Then, only in the O₃ retrieval scheme, we subtract the previously derived wavelength-dependent AOD baseline polynomial. This AOD baseline is determined by fitting a second- or third-order polynomial to nonabsorbing wavelengths in the spectral range between 400 and 870 nm (Figure 2a). The nonabsorbing wavelengths are determined from modeling a transmittance spectrum without aerosol or molecular absorption. This is done using a MODTRAN 5.2.1 simulation of a full atmospheric column transmittance, degrading the high-resolution calculated spectrum to the 4STAR resolution. Transmittance values that exceed 0.996 are considered nonabsorbing (see grey dots in Figure 2a). This baseline is then subtracted from the non-Rayleigh optical depth, yielding the input spectrum (Figure 2c) for the O₃ retrieval.

After the subtractions (Rayleigh only for NO₂ and Rayleigh and AOD baseline for O₃), we perform a least squares inversion on the following set of linear equations:

$$\begin{aligned} OD_{\lambda 1} &= c_{11}f_1 + c_{12}f_2 + c_{13}f_3 + \dots + c_{1N}f_N \\ OD_{\lambda 2} &= c_{21}f_1 + c_{22}f_2 + c_{23}f_3 + \dots + c_{2N}f_N \\ &\dots \\ OD_{\lambda M} &= c_{M1}f_1 + c_{M2}f_2 + c_{M3}f_3 + \dots + c_{MN}f_N \end{aligned} \quad (3)$$

where $OD_{\lambda i}$ is the non-Rayleigh nonaerosol (O₃ only) slant path optical depth at wavelength i (for the specified range of M wavelengths), c_{ij} is the j th component (e.g., O₃, NO₂, etc. up to N components) cross

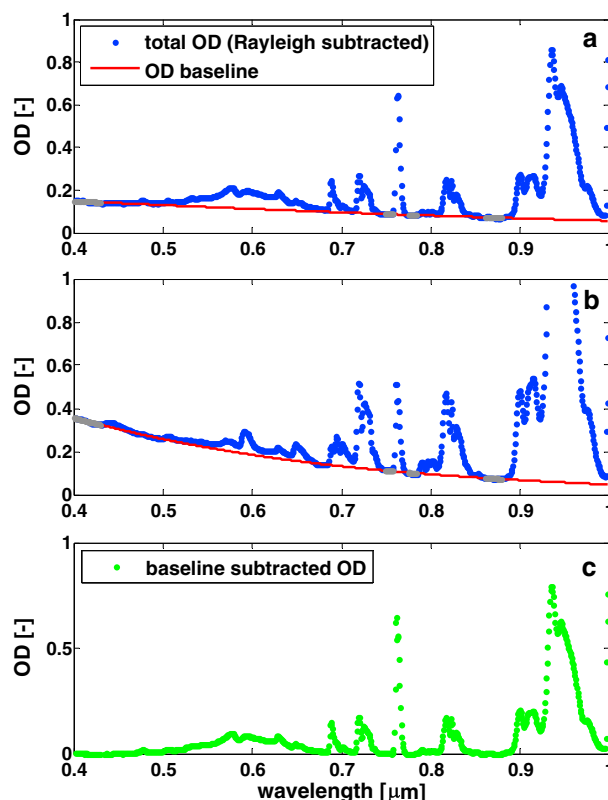


Figure 2. (a) Example of total optical depth (OD), Rayleigh subtracted, from 14 February 2013 flight, and derived second-order polynomial AOD baseline (solid red line) using only nonabsorbing wavelengths (grey dots), as explained in text; (b) as in Figure 2a but for third-order polynomial AOD baseline (solid red line); spectrum is from 17 July flight; (c) total OD after AOD baseline subtraction for 14 February example used as input for the retrieval.

section at wavelength i , and f_j is the corresponding slant column fraction of each component. Reducing equation (3) to a matrix notation and performing the inversion to get f , the slant column density of each component yields the following:

$$[f] = \text{INV}[\mathbf{C}] \times [\text{OD}] \quad \text{where } \mathbf{C} = (c_{11}, c_{12}, \dots, c_{MN}) \quad (4)$$

where $[f]$, $[\mathbf{C}]$, and $[\text{OD}]$ are arrays (matrix in bold) with the following dimensions: $[N \times 1]$, $[M \times N]$, and $[M \times 1]$.

The inverse matrix of \mathbf{C} ($\text{INV}[\mathbf{C}]$) is calculated based on singular value decomposition [Malinowski, 2002]. This method is adapted to solve systems of M equations (232 or 50 for the O_3 and NO_2 cases, respectively) and N unknowns (four gaseous components) with $M > N$. Following the above generalization, O_3 is retrieved using the Chappuis band in the spectral range between 495 and 670 nm, and NO_2 is retrieved in the spectral range between 430 and 490 nm. For both spectral regions we fit cross sections of O_3 at 223 K (interpolated from Bogumil *et al.* [2003]), NO_2 at 254 K (interpolated from Vandaele *et al.* [1998] data), $\text{O}_2\text{-O}_2$ collision induced absorption from the HITRAN database [Richard *et al.*, 2012], and water vapor at 1013 hPa and 273 K from the HITRAN database [Rothman *et al.*, 2009].

We use equation (4) to yield the best O_3

slant path amount in the spectral range of 495–670 nm, taking into account all gases stated in equation (2) and an additional linear wavelength-dependent term that accounts for any residuals remaining after the AOD baseline subtraction in the O_3 retrieval scheme. O_3 vertical column density is then calculated by dividing the total slant path by the (almost) geometric air mass derivation given by Komhyr [1980]. In our analysis of TCAP O_3 data, we found that for absorbing aerosols, which may have a strong wavelength dependency, especially in the short UV-VIS range [Barnard *et al.*, 2008], a third-order polynomial fit in the AOD spectrally dependent baseline derivation (see example spectrum from 17 July 2012 flight in Figure 2b) yields lower RMS (root-mean-square) values than does a second-order polynomial fit. Hence, for most of the TCAP summer cases that include smoke or urban pollution contributions we use a third-order polynomial for the aerosol spectral baseline derivation.

We found that using this stepwise retrieval scheme to derive O_3 columnar amounts (by first subtracting the calculated molecular (Rayleigh) component and then fitting the aerosol spectral shape before performing the least squares retrieval) is better suited to the 4STAR spectral characteristics and the spectral region used for the O_3 retrieval. This scheme is slightly different from that used in the classic differential optical absorption spectroscopy (DOAS) method [Platt and Stutz, 2008; Herman *et al.*, 2009], in which a high-order (fourth or fifth) polynomial is assigned simultaneously with all other gas cross sections to account for both the Rayleigh and the aerosol component broad absorption features. In the 4STAR case, the lower spectral resolution in comparison to other direct-Sun spectrometers, such as the MFDOAS or Pandora [e.g., Herman *et al.*, 2009] and our retrieval spectral range that covers the Chappuis O_3 band, was found to be more sensitive to the aerosol spectral shape in comparison to other instruments that use the DOAS technique and the sharply structured Huggins band (i.e., 308–326 nm) in their retrievals. Hence, utilizing the broader spectral range to derive the aerosol wavelength dependency and using it

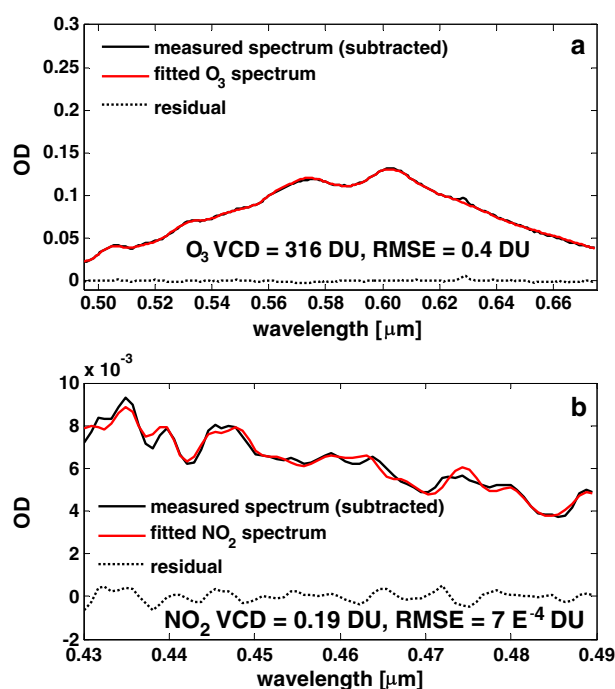


Figure 3. (a) The measured (solid black line) O_3 Chappuis band (after baseline subtraction) as shown in Figure 2c and optical depth fit (solid red line) with the reconstruction residual (black dotted line), which is the residual of the difference between the measured spectrum and the fitted (reconstructed from retrieved quantities) spectrum; the retrieved O_3 values for these instances are 316 DU, as shown in the figure; (b) the measured NO_2 spectrum (solid black line), after Rayleigh subtraction, the fitted optical depth (solid red line), as detailed in text, and the reconstruction, residual (black dotted line). The retrieved column value of NO_2 in Dobson units corresponds to 5.1×10^{15} molecules/ cm^2 .

reference spectrum approach), we have processed the TCAP winter phase data (including the Goddard campaign) using C_0 from the 14 February 2013 Langley flight, which yielded the lowest RMSD and bias values compared to the OMI stratospheric values. Using a single calibration spectrum (14 February, which yielded an RMSD of 0.07 DU for all the data compared) and not an average spectrum from the two Langley flights (12 and 14 February, which yielded an RMSD of 0.1 DU for all the data compared) is common practice in retrievals of trace gases using the DOAS method [e.g., Herman *et al.*, 2009] since it minimizes atmospheric and instrument-related changes.

O_3 and NO_2 retrieval uncertainties are determined by the root-mean-square error (RMSE) between the measured spectrum of non-Rayleigh optical depth (AOD baseline subtracted in the case of O_3) and the reconstructed spectrum from the derived coefficients for the retrieval wavelength range (232 wavelengths and 50 wavelengths for O_3 and NO_2 , respectively). The wavelength-dependent difference between the measured and reconstructed spectra is converted from OD units to Dobson units and then summed and squared to yield the integrated RMSE in Dobson units. Figures 3a and 3b show example fits for O_3 and NO_2 from 14 February 2013 during the TCAP winter campaign.

2.3. Pandora

The Pandora instrument is a ground-based direct-Sun and sky spectrometer, which can measure the direct solar irradiance in the spectral range of 265–530 nm, with a spectral resolution (FWHM) of 0.6 nm and a direct-Sun FOV of 1.6° [Herman *et al.*, 2009]. Its hyperspectral capability, its operation in the direct-Sun mode, and the ability to retrieve NO_2 and O_3 total column make it a perfect candidate for validating the 4STAR O_3 and NO_2 retrieved products. The Pandora instruments were validated in many field and intercomparison campaigns [e.g., Herman *et al.*, 2009; Tzortziou *et al.*, 2012] and are used as ground-based standard in many of the current air-quality campaigns (e.g., DISCOVER-AQ [Tzortziou *et al.*, 2013]). According to previous studies

as a priori input to the retrieval is advantageous in our case and improves our retrieval robustness and consistency.

In performing our NO_2 retrievals, we fit all the aforementioned gas cross sections (equation (2)) with a second-order (in wavelength) polynomial to describe the aerosol spectral shape over the narrow spectral range of 430–490 nm (Figure 3b). This is done for the non-Rayleigh OD, as shown in Figure 2a. NO_2 accuracy is estimated by comparing retrieved 4STAR stratospheric values (for measurements above ~ 6 km, during the Langley flights) with OMI stratospheric NO_2 for the corresponding flight paths and dates. These comparisons yielded RMS differences (RMSD) of 0.13, 0.08, and 0.08 Dobson units (DU) and biases of 0.13, 0.08, and 0.07 DU for the three corresponding Langley flights during TCAP on 22 July, 12 February, and 14 February, respectively. These RMSD and bias values correspond to typical stratospheric NO_2 levels (~ 0.1 DU) and are in accord with the Pandora accuracy level for NO_2 [Herman *et al.*, 2009].

It should be noted that since retrieved NO_2 values are sensitive to the NO_2 amount that was used in the Co derivation (as also shown by Herman *et al.* [2009] for their

[Herman *et al.*, 2009; Tzortziou *et al.*, 2012], Pandora NO₂ accuracy is about 0.1 DU, and precision is about 0.01 for cloud-free data, and O₃ accuracy is within 2 DU based on comparison with the Goddard Space Flight Center (GSFC) Brewer double monochromator.

In the following, we present results from an intercomparison ground-based campaign held at GSFC (Goddard Space Flight Center, Maryland) immediately after the completion of the TCAP winter phase in March 2013. The Pandora instruments are developed, calibrated, and deployed continuously at GSFC year-round. 4STAR-Pandora measurements were taken side by side on the GSFC laboratory roof, with 4STAR acquisition rate of 1 Hz (six averages) and Pandora of 0.05 Hz but with 4000 averages.

2.4. OMI

The OMI (Ozone Monitoring Instrument) aboard the Aura satellite employs hyperspectral imaging in a push-broom mode to observe solar backscatter radiation in the visible and ultraviolet spectral ranges. The hyperspectral capabilities improve the accuracy and precision of the total O₃ amounts and allows for the derivation of other trace gases such as NO₂. It covers a spectral range of 270–500 nm, with FWHM of 0.45–1.0 nm. The products that will be used in the ensuing analysis include total O₃, NO₂ (total and stratospheric amounts), and cloud fraction. We use OMI total column O₃ level-2 products at pixel resolution (13 × 24 km at nadir) that are based on the OMTO3 algorithm [Bhartia, 2002]. This level-2 global total column O₃ product (OMTO3) is based on the enhanced Total Ozone Mapping Spectrometer version 8 algorithm that essentially uses the ultraviolet radiance data at 317.5 and 331.2 nm. Additional OMI hyperspectral measurements help in the corrections for the factors that induce uncertainty in O₃ retrieval (e.g., cloud and aerosol, sea-glint effects, profile shape sensitivity, and SO₂ and other trace-gas contamination). For NO₂, we use the level-2 OMNO2 OMI product [Boersma *et al.*, 2002], which utilizes the DOAS fitting method over the spectral range of 405–465 nm. OMI satellite retrievals of total column NO₂ usually underestimate the amount of NO₂, especially in highly polluted regions [Tzortziou *et al.*, 2013, Figure 8]. The major factor contributing to the disagreement between OMI and Pandora is OMI's large 13 × 24 km² FOV, which can average over areas of low and high NO₂ amounts. Additional OMI algorithmic uncertainties are errors in the estimated air mass factor and errors in the assumed surface reflectivity.

2.5. TCAP Campaign

TCAP, the Two-Column Aerosol Project, aimed to provide a detailed set of observations to investigate radiation and cloud condensation closure studies, to develop new retrieval algorithms for AOD in the vicinity of clouds, and to learn about aging of anthropogenic aerosols. It was a DOE (Department of Energy) project, supported by the Atmospheric Radiation Measurement (ARM) Climate Research Facility. During the 12 month campaign period (starting in summer 2012), an ARM Mobile Facility (AMF) and a mobile aerosol observing system (MAOS) were deployed on Cape Cod, Massachusetts. During the campaign, two airborne deployments were held, based at the Hyannis airport: the first in July 2012 (summer phase) and the second in February 2013 (winter phase). 4STAR flew on the DOE Gulfstream 1 (G-1) aircraft in both phases, successfully completing its first airborne field campaign, along with a suite of in situ instruments to measure atmospheric state parameters and aerosol and cloud characteristics. The NASA B-200 aircraft participated in the summer phase only, carrying remote-sensing instruments such as the HSRL-2 (High Spectral Resolution Lidar-2). Flight patterns concentrated on two locations, the first above the ground site at the north end of the Cape (where the AMF and MAOS units were stationed) and the second at sea, usually east to southeast of the cape (see some representative flight paths shown in Figure 10). In our analysis we include data from both phases and investigate polluted air masses transported from Canada and Northern and Midwest U.S. for several of the summer phase days.

The ground-based campaign at GSFC was intended to help characterize 4STAR NO₂/O₃ measurements during TCAP and included ground-based comparison of 4STAR with several routinely deployed Pandora instruments at GSFC during 19–22 March 2013.

3. Results and Discussion

3.1. In Situ Comparison—Water Vapor

We compare retrieved CWV from 4STAR with an in situ (aboard the G-1) GE-1011B chilled mirror hygrometer to assess the instrument performance and stability during the two TCAP phases. These comparisons are constrained to spiral ascents or descents of the aircraft and include 24 such profiles from both TCAP phases.

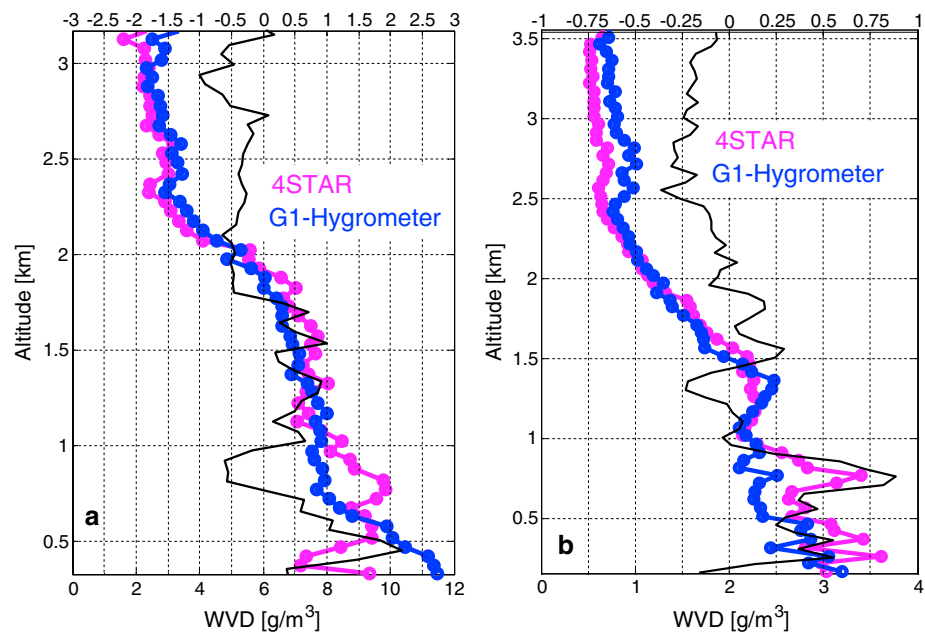


Figure 4. (a) The 4STAR (solid circle magenta line) derived water vapor density (WVD) mean profiles ($n = 20$) during TCAP summer phase, compared with G-1 hygrometer in situ measured corresponding profiles (solid circle blue line), with the difference (solid black line) between in situ and 4STAR shown on the upper x axis; and (b) same as Figure 4a except that the mean profiles are from the TCAP winter phase ($n = 13$).

To construct layer water vapor (WV) values from the G-1 hygrometer, we integrate the in situ measurements over the selected spiral leg.

Water vapor amounts (in g/cm^2) from the in situ measurement are calculated from the measured dew point temperature (GE-1011B chilled mirror, hereafter G-1 hygrometer), static temperature (Rosemount 1201 F1), and static pressure (Rosemount E102AL), as given in Bögel [1977, equations 6.5 and 17]. We derive the uncertainty in the in situ water vapor measurement by propagating the measurement uncertainty from the G-1 hygrometer (± 0.2 – 0.4°C) and the static temperature ($\pm 0.5^\circ\text{C}$) using the same conversion formula from Bögel [1977]. The total layer uncertainty is calculated as the mean uncertainty of the integrated values within the column. 4STAR layer WV values are calculated as the difference between CWV amounts at layer top and bottom for each spiral. Uncertainty is calculated for each of the layers (i.e., top and bottom), as detailed in section 2.2.1, and averaged to yield the final error bars for a given layer.

Water vapor density (WVD) (in g/m^3) profiles from the 4STAR are calculated by binning the measured CWV amounts (in g/cm^2) into 50 m layers (z in meters), followed by a spline interpolation of the binned values over the ascent/descent leg. Then, the first derivative ($\partial\text{CWV}/\partial z$) is constructed to yield WVD values along the profile. Figures 4a and 4b show the mean WVD profiles for summer ($n = 20$ profiles) and winter ($n = 13$ profiles) phases, respectively. As seen, the agreement in general is good, with an RMSD of $0.69 \text{ g}/\text{m}^3$ (12.5%) and $0.2 \text{ g}/\text{m}^3$ (13.4%) for the mean summer and winter profiles and biases of $-0.13 \text{ g}/\text{m}^3$ (-2.3%) and $0.035 \text{ g}/\text{m}^3$ (2.09%) that are distributed around zero, in most parts. Some discrepancies might result from interpolation errors (e.g., degraded resolution derivatives) or from horizontal variability at higher altitudes that only affect the 4STAR total column measurement [e.g., Schmid *et al.*, 2003; Redemann *et al.*, 2003]. Other sources of discrepancy for both mean profiles comparisons would be that the two sensors are fundamentally not observing the same air mass—in situ being sampled around the spiral while the 4STAR measurements are instantaneous direct-to-Sun views.

Figure 5 summarizes both the layer (Figure 5a) and profile (Figure 5b) comparisons. In Figure 5a we compare 22 column-integrated spiral profiles from the two TCAP phases that are deeper than 1.0 km and have valid 4STAR CWV throughout the profile. The agreement between the two instruments is characterized by a bias of $-0.045 \text{ g}/\text{cm}^2$ (-4.26%) and an RMSD of $0.28 \text{ g}/\text{cm}^2$ (26.3%). The data points corresponding to the lower left part of Figure 5a (below $1 \text{ g}/\text{cm}^2$) represent winter phase measurements. Even for very low water vapor amounts the agreement between the two instruments illustrates 4STAR's high sensitivity and retrieval

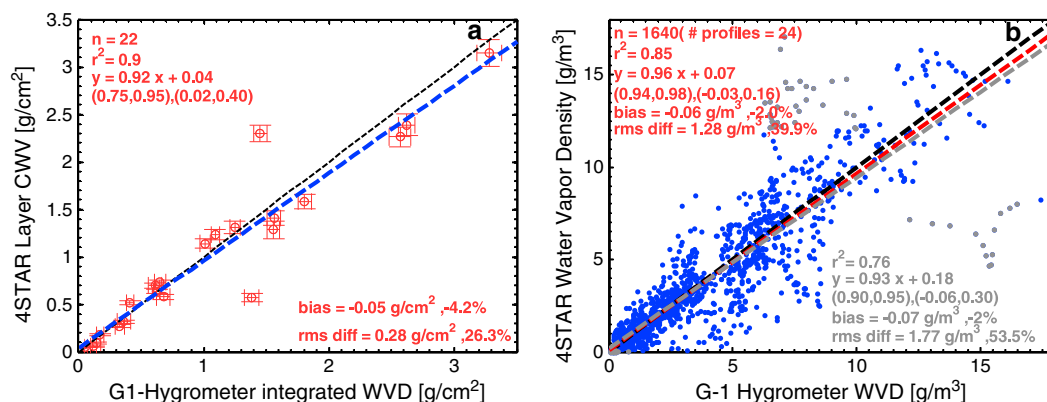


Figure 5. (a) The 4STAR layer water vapor (WV) versus integrated water vapor density (WVD) amount from G-1 hygrometer for 22 spiral profiles with valid WV layer amount during TCAP summer and winter phases (data points are marked as red circles), with fitted linear line in dashed blue (1:1 line in dashed black); error bars represent layer amount uncertainty for each of the instruments, as detailed in text. (b) The 4STAR water vapor density values, calculated from interpolating and using the first derivative of the measured column, as detailed in text, versus profile measurements (data shown is from 24 available profiles) of water vapor density from the G-1 in situ measurements. The fitted linear line (excluding biased points marked in grey) is in dashed red (corresponding statistical measures in red), fitted linear line including all data points is in grey (with corresponding statistical measures in grey), and the dashed black line is the 1:1 line. Numbers in parentheses represent the 95% confidence interval for the fitted intercepts and slopes. Biases are calculated as the mean of 4STAR minus in situ values.

robustness of CWV. An R^2 value of 0.89 indicates that the two instruments are capturing the same variability in CWV. The symbols in the upper part of the plot represent summer layer measurements, which encountered a larger range of CWV amounts than the winter measurements. This large range of summer CWV amounts can be attributed to the influence of various air mass transport and circulation patterns, as will be demonstrated later. Figure 5b shows WVD comparisons for 50 m bins over 24 available profiles. Here results are more scattered. Nevertheless, when excluding the high-biased grey dots, corresponding to strong spikes in profile comparisons (which are attributed to spline smoothing artifacts due to lack of enough data points in one or more altitude bins after 4STAR data are degraded to a vertical profile resolution of ~ 150 m), a linear 1:1 correlation is statistically significant (linear model goodness of fit test is statistically significant over the null hypothesis of median model to data), with a near-zero bias (note the 95% confidence interval of the fit in parenthesis). The absolute RMSD (excluding grey dots) is 1.38 g/m^3 , which represents a 10–30% difference between water vapor concentrations of 5 and 15 g/m^3 .

3.2. Comparison of 4STAR Measurements to Ground-Based and Satellite Observations

To evaluate the new 4STAR O_3 and NO_2 products, we compare retrieved values with OMI and Pandora. Comparisons with OMI are made for total O_3 column (corrected for flight altitude) for the two TCAP phases, and comparison with the ground-based Pandora instruments at NASA Goddard are made for both O_3 and NO_2 derived vertical column densities (VCD).

Blue and red markers in Figure 6 represent 4STAR O_3 VCD versus total columnar O_3 from OMI for most flight days during both TCAP phases. The 4STAR retrieved values shown are filtered for those that yield less than 3 DU^2 mean square error (MSE) values, augmented for the estimated below-aircraft contributions based on the climatology database mentioned in section 2.2 and are averaged within an OMI grid box of $13 \times 24 \text{ km}^2$. Since O_3 vertical variability is hard to assess without in situ measurements, flight sections that span more than 300 m change in altitude within each OMI grid are excluded from the comparison. OMI values are filtered for instances with cloud fraction less than 0.2 over the OMI grid of $13 \times 24 \text{ km}^2$. The degree of agreement (bias 3.5 DU or 1.1%, RMSD 10.6 DU or 3.1%) for both TCAP phases demonstrates the robustness of our retrieval algorithm and the instrument stability. This agreement is within the agreement range of Pandora-OMI comparison at four locations over the globe [Tzortziou et al., 2012], which yielded values between 1 and 5% for the various O_3 columns and locations.

In general, we find that O_3 VCD values are lower in summer than in winter, with average values of 314 DU and 339 DU, respectively. These average quantities seem to correspond well with the recent O_3 climatology [McPeters and Labow, 2012], which has total column values of ~ 315 DU and ~ 345 DU for latitudes between 30 and 50°N for July and February, respectively. We note the similarity to the water vapor behavior, where

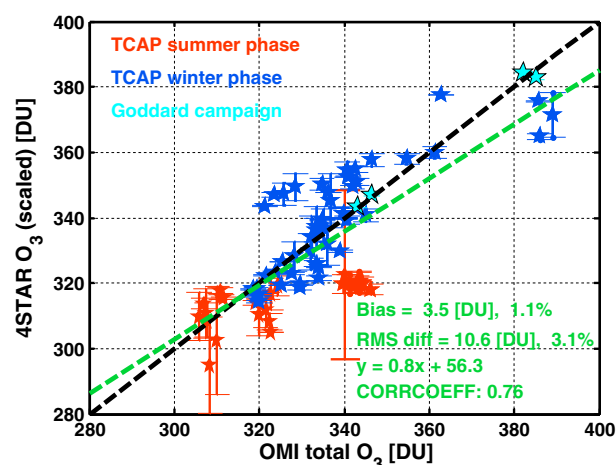


Figure 6. The 4STAR total columnar O_3 , corrected for aircraft altitude (as detailed in text) and filtered for retrieved values with MSE fitting error of less than 3 DU^2 , compared with OMI total O_3 amount for the corresponding TCAP summer/winter flight days. OMI data are considered only for instances with less than 0.2 cloud fraction within each OMI grid cell. The 4STAR values are averaged within each OMI grid cell of $13 \times 24 \text{ km}$, and only data with altitude standard deviation of less than 300 m is shown in the plot. Error bars represent standard deviation of the 4STAR averaged values within each OMI grid cell. Note that the OMI overpasses were not temporally coincident (with time lag between 1 and 3 h) with G-1 flights. RMS and bias values are calculated for the 4STAR instrument versus (minus) OMI. The dashed black line is the 1:1 line. Data points in cyan are from the ground-based comparison in Goddard in March 2013 (see Figure 7) and are collocated in time. These points represent total column from ground and, hence, are not scaled.

summer O_3 values span a broader range. The higher O_3 values range may be due to the relatively high aerosol variability that affects the AOD wavelength dependency and hence the O_3 retrieval procedure for 4STAR. Other reasons for this variability can be higher water vapor amounts that can affect the retrieval and the different calibration TOA spectra used in the separate phases. Nevertheless, bias and RMSD errors are only a few percent.

The ground-based intercomparison campaign at Goddard in March 2013 yielded even more favorable agreement (see cyan markers in Figure 6) between 4STAR and OMI columnar O_3 values, where OMI values corresponding to Goddard were taken from the daily average overpasses over Goddard (<http://avdc.gsfc.nasa.gov/index>, DATA/ AURA/ OMNO2 V03 or DATA/ AURA/ OMT03), under cloud-free conditions (i.e., cloud fraction < 0.1). The results of the airborne and ground-based comparisons of 4STAR and OMI O_3 retrievals demonstrate 4STAR's capability to yield reliable total columnar O_3 in clear sky cases and equally reliable columnar O_3 values above cloud tops in cloudy cases.

In our attempt to compare 4STAR and OMI NO_2 products, there were too few data points ($n = 3$) that passed the filter criteria of instrument altitude below 100 m and cloud free (i.e., cloud fraction < 0.2) conditions. Hence, NO_2 comparisons are made only for the ground-based intercomparison campaign at NASA Goddard, where four Pandora instruments were operated simultaneously with 4STAR from a laboratory rooftop.

Figure 7 shows time series for the three measurement days at Goddard for both O_3 and NO_2 . Measurements are taken at the same time, albeit with lower acquisition rate for the Pandora instruments (1 per 20 s). The Pandora data used in this comparison are averages of coincident measurements from all four Pandora instruments (numbers: 27, 29, 34, and 36). 4STAR and Pandora retrievals exhibit good agreement on 20 and 22 March, where conditions were partly cloudy and clear sky, respectively. On 19 March we encountered higher cloud frequency, especially after 14:00 local time, when the Pandora instruments started taking measurements. In general, we find that the 4STAR retrievals follow the Pandora time series closely both for O_3 and for NO_2 and agree well with corresponding near-coincident OMI O_3 and NO_2 total column measurements when the latter were available. Since O_3 and NO_2 values from the 22 March OMI overpass are not available, the OMI values in the figure are averages of the 21 and 23 March OMI retrievals.

Figure 8a presents a 4STAR-Pandora correlation plot for the 3 days. To calculate correlations, results from both instruments are interpolated onto an evenly spaced time grid within the coincident measurement period. The RMSD for all 4STAR-Pandora O_3 data points is 5.03 DU (1.3%), and bias is 1.66 DU (0.6%). Filtered data are screened using first derivative product of the retrieved O_3 values and their corresponding fit MSE, which are allowed to deviate by no more (or less) than the mean values plus (or minus) 2 SD, and yielded RMSD of 3.79 DU (1%) and bias of 0.14 DU (0.1%). In general, this compares well with results obtained by Pandora-Brewer ground-based comparisons [Tzortziou *et al.*, 2012], which showed RMSD of 1–1.3% (1–5 DU, depending on total column amounts) at various geographic locations, at different seasons. Nevertheless, we see that on the cloudy day (19 March) and on the partly cloudy day (20 March) there is a bias between the two instruments. It might be that due to the 4STAR retrieval scheme, which uses the broad-featured Chappuis band, partial

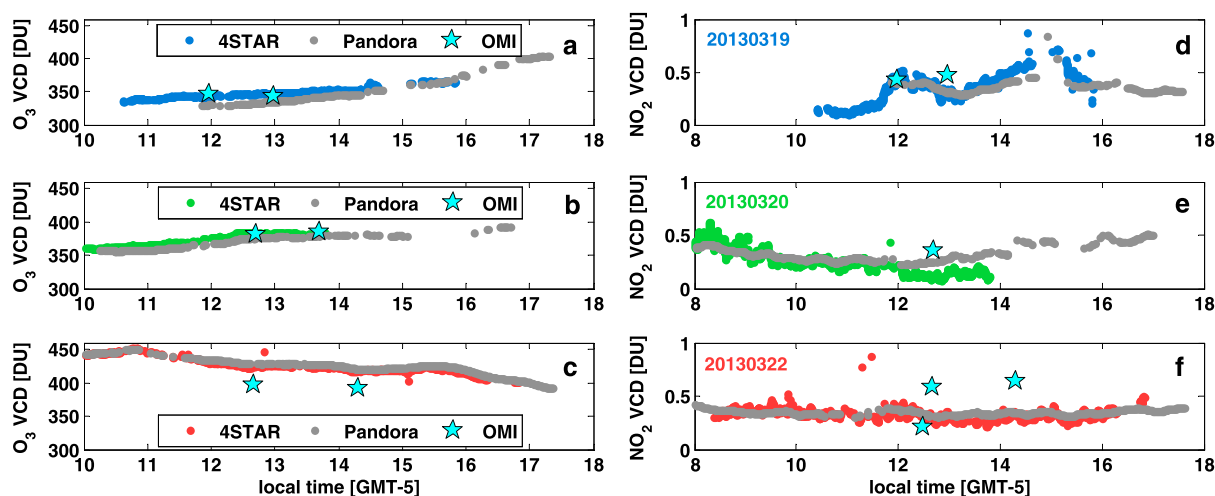


Figure 7. (a–c) The 4STAR O_3 and (d–f) NO_2 retrieved vertical column densities (VCD) compared with collocated, averaged values of four Pandora instruments (#27, 29, 34, and 36) during the March 2013 Goddard ground-based intercomparison period and with OMI overpass values (in cyan stars).

obscuration by clouds has larger effects on the retrieved amounts. This is in contrast to the retrieval approach that uses the sharp O_3 spectral features, as in the case of the Pandora [Tzortziou *et al.*, 2012]. Longer intercomparison periods are needed to establish a better understanding of 4STAR biases and instrument performance under various atmospheric conditions and seasons. In Figure 8b we show the NO_2 comparison, including all data points and filtered data. Filter criteria are similar to those used for O_3 . All data points yield RMSD of -0.05 DU (18.2%) and bias of -0.01 DU (-5.5%). Filtered data points yield RMSD of 0.05 DU (17.4%) and bias of -0.02 DU (-7.9%), and a better correlation coefficient of 0.81 (versus 0.67 for all data). These RMSD and bias values are within the range of the instrument NO_2 accuracy (~ 0.1 DU on average) and also correspond well with the Pandora accuracy of 0.1 DU for NO_2 [Herman *et al.*, 2009]. In the following section we extend the application of 4STAR water vapor, O_3 , and NO_2 retrieved values to infer the characteristics and origin of elevated pollution layers observed during the TCAP summer phase.

3.3. Elevated Pollution Layers

An inherent capability of 4STAR and its predecessor AATS-14 is to measure total columnar composition above the instrument (i.e., aircraft). This allows remote measurements of aerosol layers above low clouds, and even stratospheric aerosols as was shown in Russell *et al.* [1996] for the post-Pinatubo eruption period. This

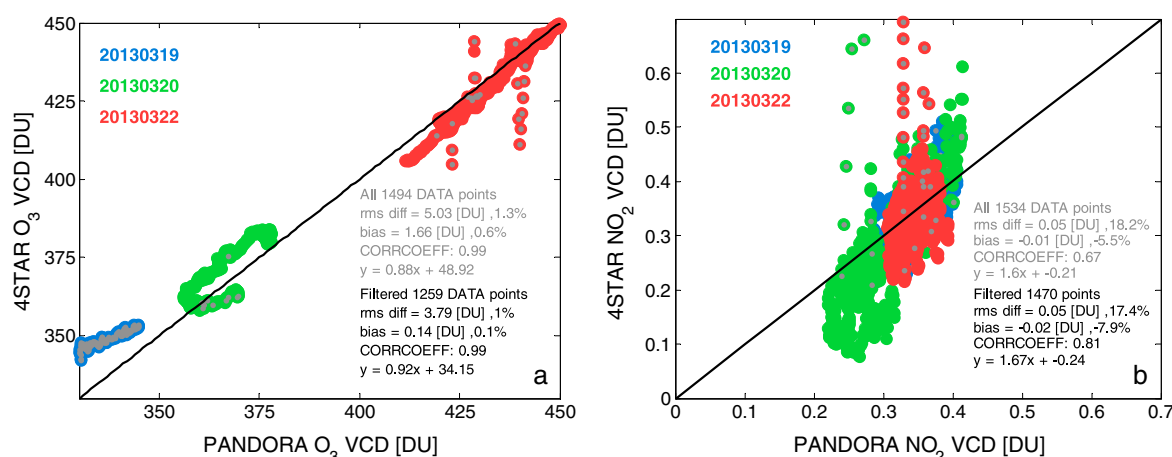


Figure 8. (a) The 4STAR-Pandora O_3 correlation plot, for the GSFC ground-based campaign; data points are colored according to measurement day. Statistical summary is given in grey for all data points and in black for filtered (including cloud and instantaneous or instrument interferences, as detailed in text) data points; (b) same as in Figure 8a except that values shown are for 4STAR-Pandora NO_2 correlation plot.

capability is extended with 4STAR and includes measurements of O_3 and NO_2 columns above the instrument. The combination of trace-gas composition and aerosol loadings and properties is used here to identify air mass composition, which can then be linked with source attribution of the specific air mass observed aloft, even in cases where the aerosol signals are relatively weak for other remote-sensing platforms to classify. Specifically, the 4STAR total column measurements above the planetary boundary layer (PBL) (i.e., above 3000 m) are used here to infer atmospheric composition of elevated pollution layers transported from the continental U.S. and Canada during the TCAP summer phase according to their total column aerosol and trace-gas amounts. This approach is desirable in cases where in situ measurements are not available. For example, on many occasions, long-range transport pollution layers are present at altitudes well above the measuring platform (either ground-based or airborne), which has consequences on atmospheric composition and radiation effects [e.g., Redemann *et al.*, 2006]. Another application of such an analysis is to demonstrate the feasibility of total column measurements in interpreting and labeling different atmospheric composition scenarios and its possible extension from airborne total column to spaceborne observations. The latter offer coverage over larger areas and longer temporal scales than those of in situ measurements made within suborbital campaigns. Since 4STAR has the proven capability to retrieve both aerosol [Shinozuka *et al.*, 2013] and trace gases such as the ones measured by OMI, it can form a useful “bridge” in understanding the link between in situ and total column spaceborne measurements of various pollution plumes. To perform our analysis, we take the 4STAR retrieved values of AOD at 500 nm, Ångström exponent (AE) at 500 nm [Shinozuka *et al.*, 2013], CWV, and NO_2 and use them as variables in a *k*-means clustering algorithm to determine the atmospheric composition characteristics of the observed elevated polluted layers during the 9, 17, 18, 21, 22, and 25 July flights. The *k*-means procedure yields a number of centroids for a given data set by minimization of the distance of the cluster centroids to each data point and the minimization of the cluster within variance [Hartigan, 1975]. The only arbitrary input needed for this calculation is the number of clusters. In our case, we use the four variables mentioned above and three clusters. In performing our analysis, we ran the *k*-means algorithm by varying the cluster number from two to five. Ultimately, we chose to use three clusters since this was the minimum number of clusters that showed distinct group features and also resulted in the minimum sum of the distances of data points from cluster centers. Indeed, with increasing cluster number, we get a reduction in the overall sum of distances of the data points from the cluster centers. However, the difference between feature ranges for each of the new groups is then decreased and the physics and chemical features become more complicated to interpret without additional measurements or modeling efforts.

Since the *k*-means procedure starts from random cluster centers, we perform 50 runs and choose the result that minimizes the sum of data points distance from the final cluster centroids. To choose our feature parameters, we have excluded each (i.e., AOD, AE, O_3 , NO_2 , and CWV), one at a time, for each series of *k*-means runs and calculated the sum of the distances between all data points and cluster centers. We found that O_3 , when included as a parameter, increases the sum distance, whereas all other parameters tend to decrease this sum. This result might be related to the fact that O_3 levels are dominated by the stratospheric values, so that the retrieved concentrations for the analyzed data points are not statistically different within the different groups and, hence, do not add more information about the different pollution layers. However, the extension of such an analysis method to a larger geographical region, which includes both source and target locations, might result in having O_3 levels significant in assessing the various atmospheric composition groups present. It should be noted that in the current case study, the retrieved NO_2 amounts (above PBL) are much higher than the stratospheric background values of ~ 0.1 DU and, hence, are chosen as one of the parameters in our analysis.

The number of data points that are used in our analysis is 1626, which includes only data above 3000 m, with valid retrievals for all four parameters, from the TCAP summer flight days detailed above.

In Figure 9 we show our clustering analysis results and the corresponding mean and range values for each of the parameters over the three groups. The number of data points in each of the groups is shown on the right *y* axis. We see that Group 1 values of AOD, AE, NO_2 , and CWV tend to exceed those of Group 2. Group 3 has low AOD values but significantly higher NO_2 and CWV amounts when compared to Group 2. Figure 10 shows that Group 1 appears along the flight paths of 17 July (near land), 18 July (ocean column), and 22 July (near land). We attribute the almost nonphysical, very high AE values of Group 3 to the very low AOD values (< 0.05 near 500 nm) that represent this Group, which result in high uncertainty in the AE derivation. We also see that Group 3 is located along the flight path of 17 July, albeit with lower AOD values. This cluster has very high NO_2 values but low AOD levels, which are probably a result of higher heterogeneity in aerosol fields over the flight

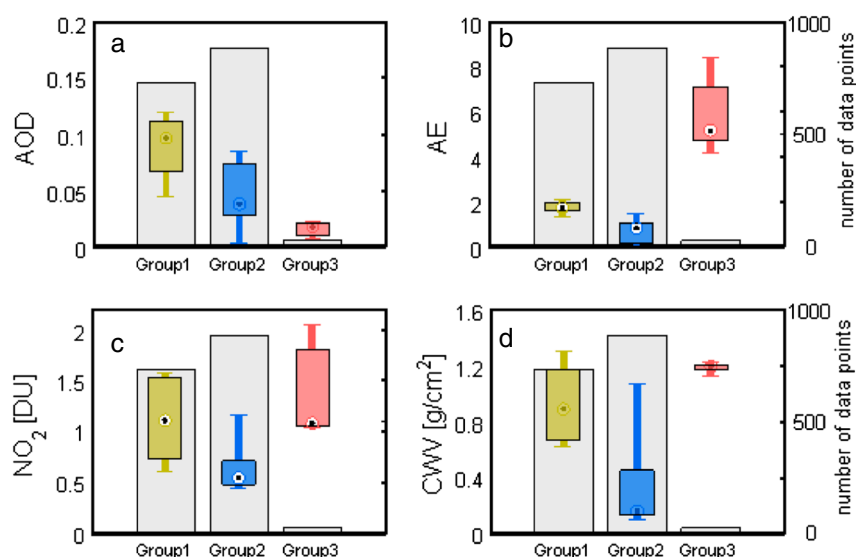


Figure 9. Box plot showing three clustered groups after performing *k*-means clustering procedure as detailed in text, using four parameters: (a) aerosol optical depth (AOD), (b) Ångström exponent (AE), (c) NO₂ concentration (in Dobson units), and (d) columnar water vapor (CWV) amount in g/cm², for total columns above flight altitude of 3000 m. Right y axis shows the number of data points in each of the groups.

region [e.g., Shinozuka and Redemann, 2011]. The latter is in contrast to the relatively stable behavior of the NO₂ and water vapor amounts, which continue to show higher values, similar to the ones that characterize Group 1.

When calculating the Wilks overall Lambda parameter, which is a measure of the within-Group covariance compared to the overall data covariance and indicates how well the input data lend themselves to separation into classes (as detailed in Burton *et al.* [2012] and Hill and Lewicki [2007]), we get an overall value of 0.104, which reflects a good separation of the defined groups shown in Figure 9.

When looking at regions a and b in Figure 10, we see that these regions correspond to Group 1 and Group

3, respectively. Both groups are characterized by high NO₂, CWV, and AE values, whereas Group 3 is characterized by much lower AOD amounts above the aircraft. Comparing qualitatively to observations obtained by the HSRL-2 [Hair *et al.*, 2008; Burton *et al.*, 2013] and to the measurements obtained by miniSPLAT, a miniaturized version of SPLAT II, single-particle mass spectrometer [Zelenyuk *et al.*, 2009], during the 17 July flight, we find good agreement with our results: region a is characterized by high measured backscatter values between 3 and 4 km (not shown) and also shows relatively high (> 5%) nitrate and biomass-burning (BB) fraction measured by miniSPLAT (Figure 11). The main differences observed between Group 1 (regions a, c, and e) and Group 3 (region b) are that the latter shows no nitrates and more aged soot in the miniSPLAT analysis and very low signal above the boundary layer (i.e., due to low AOD levels) with HSRL data. Nevertheless, our analysis succeeds in identifying this

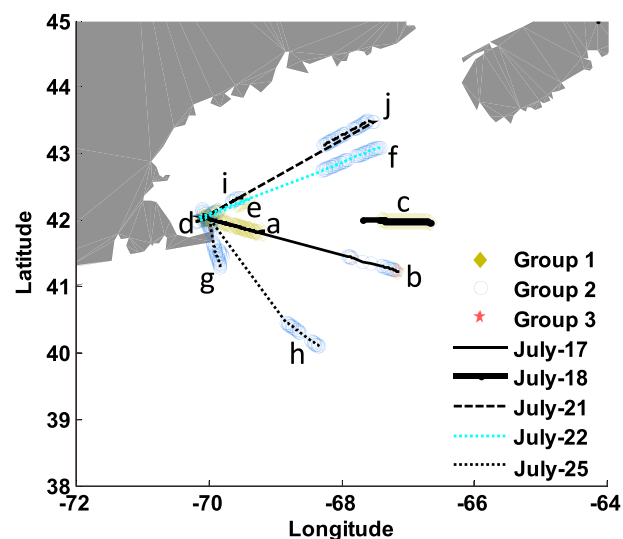


Figure 10. The *k*-means cluster analysis results for TCAP summer phase campaign (for constant legs above 3000 m) underlying corresponding flight path. Group characteristics correspond to number and group color shown in Figure 9. Lowercase letters correspond to starting points along flight path of Hysplit 48 h back trajectory simulations, which are shown in Figure 12.

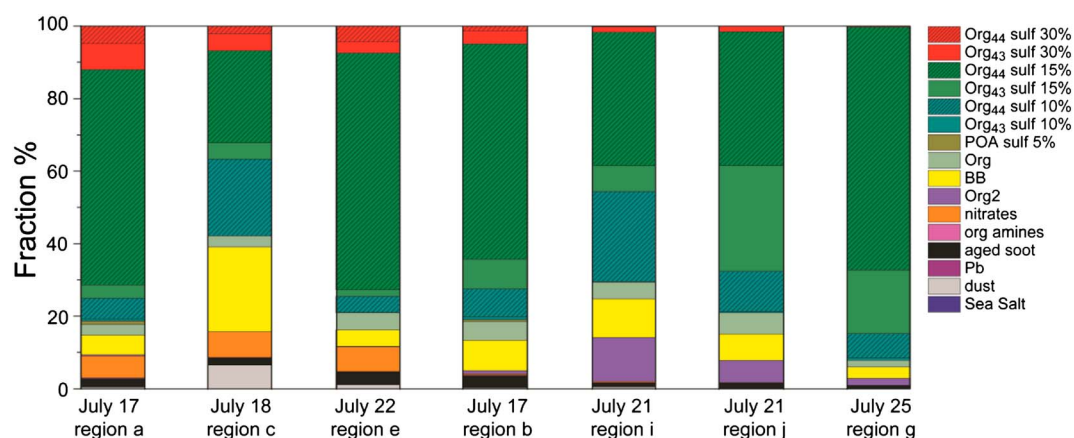


Figure 11. Composition of individual aerosol particles characterized by single-particle mass spectrometer, miniSPLAT, during selected time intervals on 17, 18, and 22 July (regions a, c, and e corresponding to Group 1 and b corresponding to Group 3 in Figure 10). Bar plots show the number fraction of particles with different compositions/mixing states as indicated in the figure legend. Mixtures of oxygenated organics and sulfate are labeled by the fraction of sulfates (10, 15, or 30%) and the dominant mass spectral peak ($m/z = 44$ or 43).

region separately despite the low AOD amounts. It should also be noted that in a comparison of Weather Research Forecast Chemistry (WRF-Chem) model output with measured quantities during the 17 July flight, the model underestimated AOD and nitrates (J. Fast, personal communication, 2013), which further strengthens the use of such an approach in detailed assessments of atmospheric composition.

The higher NO_2 values and low nitrate content assigned with Group 3 (see Figure 9c) might imply less NO_2 oxidation associated with these data points. Aerosol type classification by HSRL-2 [Burton *et al.*, 2012, 2013] for the 17 July flight shows mostly urban pollution aerosol at the land column (region a), which are usually characterized by high NO_2 values [e.g., Herman *et al.*, 2009; Oetjen *et al.*, 2013], and corresponds well with our analysis. The 18 July flight (region c in Figure 10) and the 22 July flight (region e in Figure 10), which belong to Group 1, with corresponding high AOD, NO_2 , and CWV values, show as well high BB and nitrate percentages measured by the miniSPLAT and further support our classification results. These regions are classified as urban pollution by the HSRL-2, albeit with very low aerosol loading. The separation between urban/BB pollution in regions a, c, e, b, and other pollution (regions f–j) by our clustering analysis corresponds well with the miniSPLAT composition analysis shown in Figure 11, whereas the former contains more sulfate, nitrate, and soot, and the latter contains more oxygenated organic with higher organic content (i.e., 85% and 90%) and carboxylic acid fraction ($m/z = 44$), which usually characterize natural biogenic emission sources.

If we examine Group 2 composition bars (Figure 11, regions i, j, and g), Org and Org2 have very distinct mass spectra, with the former being dominated by oxygenated organics and the latter having characteristic mass spectral peaks at $m/z = 80$, 53, and 27. The different amount of Org/Org2 within Group 2 might imply further division into subgroups of these pollution sources (as was observed when running cases with $k = 4/5$), but additional laboratory and modeling analysis is needed to determine the exact chemical composition and the correct labeling of each pollution plume for each of the regions in order to further assess their possible source origins and characteristics, as they reflect with the 4STAR retrieved properties.

Further, to apply a broader perspective to our clustering analysis, we have performed back trajectory analyses by Hysplit (Hybrid Single-Particle Lagrangian Integrated Trajectory Model [Draxler and Rolph, 2013]). These are presented in Figure 12 and show distinct differences between the air masses encountered on 17, 18, and 22 July and on the 21 and 25 July flights (and also 9 July path, which overlays partly the 25 July flight path and is not shown for clarity of the plot). On 17, 18, and 22 July, the 48 h back trajectories from levels of 3500 (shown in figure), 4500, and 5500 m indicated the transport of air masses from Mid-northern U.S. As detailed in Table 1, these trajectories intersected atmospheric levels between 0 and 3000 m and are characterized by high relative humidity (RH) values, as also confirmed by high CWV values measured by 4STAR.

When examining MODIS real-time fire product maps (MODIS Rapid Response Fire website: <http://rapidfire.sci.gsfc.nasa.gov/cgi-bin/imagery>) for the period of 9 through 29 July, we found that these trajectories might

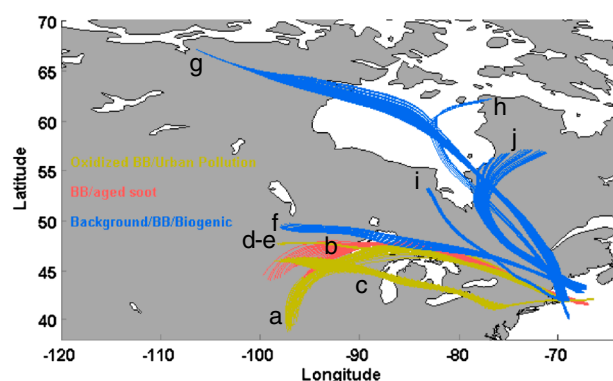


Figure 12. Forty-eight-hour back trajectories from flight locations, corresponding to the groups shown in Figure 10. Trajectories starting levels correspond to the constant altitude flight legs and some additional altitudes, as detailed in Table 1.

have been affected by fires in the midwest and northern U.S. The miniSPLAT measurement from the 17, 18, and 22 July flights shown in Figure 11 and the high AE values corresponding to Group 1 plausibly support the fact that these air masses contain smoke from midwest U.S., in addition to urban pollution from the eastern coast of the U.S. In contrast, 9 (not shown), 21, and 25 July back trajectories show air masses transported from Canada. These air masses originate at higher tropospheric layers (above 5500 m) for both land and ocean columns and are characterized by very low RH values ($\sim 10\%$), with high amounts of organic compounds, and do not show a distinct urban pollution signature (as

implied from the relatively low NO_2 and CWV values associated with them). The BB content and relatively high fraction of rather uncommon organic compounds (Org2) observed within these air masses (i.e., Group 2) might imply a more complex history that includes fires and biogenic emissions that could benefit from a more detailed laboratory and modeling analysis. Some planned future retrieval capabilities of 4STAR, such as formaldehyde column amounts, could likely contribute further to this type of analysis.

The back trajectory path that corresponds to the 22 July ocean column (region f in Figures 10 and 12) shows air that passes through the northern part of the U.S. but nevertheless is identified as part of Group 2. We see that RH levels of these air masses are low ($\sim 20\text{--}30\%$) and originate from levels above 2500 m, as in the other regions corresponding to Group 2. This might explain the relatively low AOD and NO_2 values that correspond to the Group 2 cluster, but it does not absolutely reject the possibility of mixed, more complicated source-attributed air masses within this group.

In summary, we find that even for very low AOD amounts above the boundary layer, where pollution is difficult to observe by other remote-sensing instruments, our approach led to the identification of different pollution clusters associated with BB and urban pollution outflow. The various clusters (i.e., Groups 1–3) corresponded

well with the analysis made by the miniSPLAT, with each group having its own chemical composition characteristics (as shown in Figure 11). Also, back trajectory analysis further confirmed that Groups 1 and 3 were separated in source origin from Group 2. A more detailed analysis supported by additional chemical analysis and modeling is needed in order to properly label the three groups defined by our analysis and to cast more light on the variability observed within Group 2. Using a similar approach on a larger data set covering more geographical regions (which might include signals from different emission sources and their target areas) could assist in identification of specific and

Table 1. Forty-Eight-Hour Back Trajectories Altitude Ranges for the Corresponding Regions Shown in Figures 10 and 12

| Region/Flight Date | End Altitude (m agl ^a) | Trajectory Altitude Range (m agl ^a) |
|--------------------|------------------------------------|---|
| N/A; 9 July 2012 | 4000 | 4000–7000 |
| a; 17 July 2012 | 5500 | 2500–5500 |
| | 4500 | 0–4500 |
| | 3500 ^b | 500–3500 |
| b; 17 July 2012 | 3500 | 2000–3500 |
| c; 18 July 2012 | 4000 | 3000–4500 |
| i; 21 July 2012 | 3500 ^b | 3500–5500 |
| | 3000 | 3000–5500 |
| j; 21 July 2012 | 4000 | 4000–7000 |
| | 3500 ^b | 3500–6500 |
| d, e; 22 July 2012 | 3500 | 2000–3500 |
| f; 22 July 2012 | 3700 ^b | 2000–3700 |
| | 3500 | 1500–3500 |
| g; 25 July 2012 | 3500 | 3500–6500 |
| | 3000 ^b | 3000–5500 |
| h; 25 July 2012 | 3500 | 3500–6000 |

^aAbove ground level.

^bWhen more than one end altitude is given for this region/date, this symbolizes the corresponding constant leg aircraft altitude.

unique features of atmospheric composition that are linked with the various source emissions and their subsequent atmospheric processes. In fact, we are currently using our approach in analyzing the SEAC⁴RS (Studies of Emissions and Atmospheric Composition, Clouds and Climate Coupling by Regional Surveys) data set, which includes a variety of smoke sources and ages, together with urban-industrial pollution and biogenic emissions.

4. Summary and Conclusions

High sensitivity and data acquisition frequency of 4STAR when measuring in the direct-Sun-tracking mode (and hence low air mass uncertainties) make it an excellent tool for O₃, water vapor, and NO₂ measurements in fast-changing environments that are affected by pollution outflow and long-range transport of smoke. In fact, this is the first time that continuous O₃ and NO₂ data have been retrieved from direct-Sun mode airborne Sun photometer measurements. Our retrieval approach follows some well-established procedures and also includes some modifications to the classic DOAS retrieval method, which is used in many remote-sensing trace-gas applications. Specifically, we utilize the broad spectral range of the 4STAR to derive the aerosol spectral shape as a first step and input this in our retrieval procedure to yield the subtracted spectrum with only gases of interest. We demonstrate here the stability and capability of the instrument to detect trace gases and compared 4STAR retrieved measurements with collocated observations of in situ airborne hygrometer for water vapor and ground-based Pandora instruments and OMI satellite retrievals for O₃ and NO₂. We show that 4STAR compares well with these instruments during the two TCAP airborne phases and during a ground-based intercomparison campaign at Goddard. Atmospheric composition remote-sensing applications are also demonstrated with the new instrument. We show that by combining the measured values of AOD, retrieved spectral dependence (AE), NO₂, and water vapor, we can differentiate between air masses with various compositions transported from different regions using a relatively simple clustering approach. Comparing our unsupervised clustering analysis with in situ miniSPLAT measurements onboard the G-1, HSRL total column measurements, and back trajectory analysis, we found that our group clusters correspond well with the additional available auxiliary data. Extending this type of analysis can become valuable when more pollution sources and types are available, together with a larger suite of in situ measurements that can confirm our total column observations. Such analysis might be considered a first step in linking in situ suborbital measurements with total column aerosol and trace-gas measurements and can be extended further to total column spaceborne observations.

Future maturation of 4STAR columnar trace-gas retrieval capabilities to detect other gases such as formaldehyde could further enhance its contribution to climate change and atmospheric composition studies.

Acknowledgments

TCAP was funded by the DOE ARM Program. We thank the ARM Aerial Facility staff for carrying out the TCAP research flights. We also thank the NASA Langley Research Center HSRL team and B200 flight crew for providing the HSRL measurements and classification products. 4STAR hardware and science algorithm development were funded by the NASA Radiation Science Program. Further maturation of 4STAR was funded by the DOE ARM program as well as the participation of 4STAR in TCAP and subsequent basic analyses. Michal Segal Rozenhaimer would like to thank the Oak Ridge Associated Universities (ORAU) administered NASA Postdoctoral program (NPP) for their financial support and the Weizmann Institute of Science in Israel for their financial support through the Women in Science Fellowship award.

References

- Ammann, M., M. Kalberer, D. T. Jost, L. Tobler, E. Rossler, D. Piguet, H. W. Gaggeler, and U. U. Baltensperger (1998), Heterogeneous production of nitrous acid on soot in polluted air masses, *Nature*, **395**, 157–160.
- Barnard, J. C., R. Volkamer, and E. I. Kassianov (2008), Estimation of the mass absorption cross section of the organic carbon component of aerosols in the Mexico City Metropolitan Area, *Atmos. Chem. Phys.*, **8**, 6665–6679.
- Bhartia, P. K. (2002), *OMI Algorithm Theoretical Basis Document*, OMI ozone products, vol. II, NASA Goddard Space Flight Center, Greenbelt, Maryland, USA.
- Boersma, F., E. Bucsela, E. Brinksma, and J. F. Gleason (2002), NO₂ retrieval algorithm, in *OMI Algorithm Theoretical Basis Document*, vol. V, pp. 13–26, Cambridge, MA.
- Bucholtz, A. (1995), Rayleigh-scattering calculations for the terrestrial atmosphere, *Appl. Opt.*, **34**, 2765–2773.
- Bögel, W. (1977), Neue Näherungsgleichungen für den Sättigungsdruck des Wasserdampfes und für die in der Meteorologie gebräuchlichen Luftfeuchte-Parameter, *DLR-FB 77-52*, Dtsch. Forsch. und Versuchsanst. für Luft- und Raumfahrt, Oberpfaffenhofen, Germany.
- Bogumil, K., et al. (2003), Measurements of molecular absorption spectra with the SCIAMACHY pre-flight model: Instrument characterization and reference data for atmospheric remote-sensing in the 230–2380 nm region, *J. Photochem. Photobiol., A*, **157**, 167–184.
- Burling, I. R., et al. (2010), Laboratory measurements of trace gas emissions from biomass burning of fuel types from the southeastern and southwestern United States, *Atmos. Chem. Phys.*, **10**, 11,115–11,130, doi:10.5194/acp-10-11115-2010.
- Burling, I. R., R. J. Yokelson, S. K. Akagi, S. P. Urbanski, C. E. Wold, D. W. T. Griffith, T. J. Johnson, J. Reardon, and D. R. Weise (2011), Airborne and ground-based measurements of the trace gases and particles emitted by prescribed fires in the United States, *Atmos. Chem. Phys.*, **11**, 12,197–12,216, doi:10.5194/acp-11-12197-2011.
- Burton, S. P., R. A. Ferrare, C. A. Hostetler, J. W. Hair, R. R. Rogers, M. D. Obland, C. F. Butler, A. L. Cook, D. B. Harper, and K. D. Floyd (2012), Aerosol classification using airborne High Spectral Resolution Lidar measurements—Methodology and examples, *Atmos. Meas. Tech.*, **5**, 73–98, doi:10.5194/amt-5-73-2012.
- Burton, S. P., R. A. Ferrare, M. A. Vaughan, A. H. Omar, R. R. Rogers, C. A. Hostetler, and J. W. Hair (2013), Aerosol classification from airborne HSRL and comparisons with the CALIPSO vertical feature mask, *Atmos. Meas. Tech.*, **6**(5), 1397–1412, doi:10.5194/amt-6-1397-2013.
- Cede, A. (2012), *Manual for Pandora Software Suite*, version 1.5. [last update November 2012.]
- Clough, S. A., M. W. Shephard, E. J. Mlawer, J. S. Delamere, M. J. Iacono, K. Cady-Pereira, S. Boukabara, and P. D. Brown (2005), Atmospheric radiative transfer modeling: A summary of the AER codes, *J. Quant. Spectrosc. Radiat. Transfer*, **91**, 233–244.

- Draxler, R. R., and G. D. Rolph (2013), HYSPLIT (Hybrid Single-Particle Lagrangian Integrated Trajectory) Model access via NOAA ARL READY Website (<http://www.arl.noaa.gov/HYSPLIT.php>), NOAA Air Resources Laboratory, College Park, MD.
- Dunagan, S. E., R. Johnson, J. Zavaleta, P. B. Russell, B. Schmid, C. Flynn, J. Redemann, Y. Shinozuka, J. Livingston, and M. Segal-Rosenheimer (2013), 4STAR spectrometer for sky-scanning Sun-tracking atmospheric research: Instrument technology, *Remote Sens.* (Special Issue "Optical Remote Sensing of the Atmosphere"), 5, 3872–3895, doi:10.3390/rs5083872.
- Dupont, R., et al. (2012), Attribution and evolution of ozone from Asian wild fires using satellite and aircraft measurements during the ARCTAS campaign, *Atmos. Chem. Phys.*, 12, 169–188, doi:10.5194/acp-12-169-2012.
- Finlayson-Pitts, B. J., and J. N. Pitts (2000), *Chemistry of the Upper and Lower Atmosphere, Theory, Experiments and Applications*, pp. 270–272, Academic Press, San Diego, CA.
- Hair, J. W., C. A. Hostetler, A. L. Cook, D. B. Harper, R. A. Ferrare, T. L. Mack, W. Welch, L. R. Izquierdo, and F. E. Hovis (2008), Airborne High Spectral Resolution Lidar for profiling aerosol optical properties, *Appl. Optics*, 47(36), 6734–6752, doi:10.1364/AO.47.006734.
- Hartigan, J. A. (1975), *Clustering Algorithms*, pp. 351, John Wiley, Hoboken, N. J.
- Herman, J., A. Cede, E. Spinei, G. Mount, M. Tzortziou, and N. Abuhassan (2009), NO₂ column amounts from ground-based Pandora and MDOAS spectrometers using the direct-Sun DOAS technique: Intercomparisons and application to OMI validation, *J. Geophys. Res.*, 114, D13307, doi:10.1029/2009JD011848.
- Hill, T., and P. Lewicki (2007), *STATISTICS Methods and Applications*, StatSoft, Tulsa, OK.
- Holben, B. N., et al. (2001), An emerging ground-based aerosol climatology: Aerosol optical depth from AERONET, *J. Geophys. Res.*, 106, 12,067–12,097.
- Ingold, T., B. Schmid, C. Matzler, P. Demoulin, and N. Kampfer (2000), Modeled and empirical approaches for retrieving columnar water vapor from solar transmittance measurements in the 0.72, 0.82 and 0.94- μ m absorption bands, *J. Geophys. Res.*, 105(D19), 24,327–24,344.
- Kasten, F. (1965), A new table and approximation formula for the relative optical air mass, *Meteorol. Geophys. Bioklimatol., Series, B14*, 206–223.
- Kasten, F., and A. T. Young (1989), Revised optical air mass tables and approximation formula, *Appl. Opt.*, 28(22), 4735–4738.
- Komhyr, W. D. (1980), Operations handbook—Ozone observations with a Dobson spectrophotometer, *Global Ozone Res. Monit. Proj. Rep.* 6, pp. 125, World Meteorol. Organ., Geneva, Switzerland.
- Livingston, J. M., et al. (2005), Retrieval of ozone column content from airborne Sun photometer measurements during SOLVE II: Comparison with coincident satellite and aircraft measurements, *Atmos. Chem. Phys.*, 5, 2035–2054.
- Livingston, J., et al. (2007), Comparison of water vapor measurements by airborne Sunphotometer and near-coincident in situ and satellite sensors during INTEX/ITCT 2004, *J. Geophys. Res.*, 112, D12S16, doi:10.1029/2006JD007733.
- Malinowski, E. R. (2002), *Factor Analysis in Chemistry*, 3rd ed., John Wiley Inc., New York.
- McPeters, R. D., and G. J. Labow (2012), Climatology 2011: An MLS and sonde derived ozone climatology for satellite retrieval algorithms, *J. Geophys. Res.*, 117, D10303, doi:10.1029/2011JD017006.
- Platt, U., and J. Stutz (2008), *Differential Optical Absorption Spectroscopy: Principles and Applications (Physics of Earth and Space Environments)*, Springer-Verlag, Berlin, Heidelberg.
- Oetjen, H., S. Baidar, N. A. Krotkov, L. N. Lamsal, M. Lechner, and R. Volkamer (2013), Airborne MAXDOAS measurements over California: Testing the NASA OMI tropospheric NO₂ product, *J. Geophys. Res. Atmos.*, 118, 7400–7413, doi:10.1002/jgrd.50550.
- Redemann, J., S. J. Masonis, B. Schmid, T. L. Anderson, P. B. Russell, J. M. Livingston, O. Dubovik, and A. D. Clarke (2003), Clear-column closure studies of aerosols and water vapor aboard the NCAR C-130 during ACE-Asia, 2001, *J. Geophys. Res.*, 108(D23), 8655, doi:10.1029/2003JD003442.
- Redemann, J., P. Pilewskie, P. B. Russell, J. M. Livingston, S. Howard, B. Schmid, J. Pommier, W. Gore, J. Eilers, and M. Wendisch (2006), Airborne measurements of spectral direct aerosol radiative forcing in the Intercontinental chemical Transport Experiment/Intercontinental Transport and Chemical Transformation of anthropogenic pollution, 2004, *J. Geophys. Res.*, 111, D14210, doi:10.1029/2005JD006812.
- Richard, C., et al. (2012), New section of the HITRAN database: Collision-induced absorption (CIA), *J. Quant. Spectrosc. Radiat. Transfer*, 113, 1276–1285.
- Rothman, L. S., et al. (2009), The HITRAN 2008 molecular spectroscopic database, *J. Quant. Spectrosc. Radiat. Transfer*, 110(9–10), 533–572.
- Russell, P. B., et al. (1996), Global to microscale evolution of the Pinatubo volcanic aerosol derived from diverse measurements and analyses, *J. Geophys. Res.*, 101, 18,745–18,763.
- Russell, P. B., et al. (2005), Aerosol optical depth measurements by airborne Sun photometer in SOLVE II: Comparisons to SAGE III, POAM III and airborne spectrometer measurements, *Atmos. Chem. Phys.*, 5, 1311–1339.
- Schmid, B., and C. Wehrli (1995), Comparison of Sun photometer calibration by use of the Langley technique and the standard lamp, *Appl. Opt.*, 34(21), 4500–4512.
- Schmid, B., K. J. Thome, P. Demoulin, R. Peter, C. Matzler, and J. Sekler (1996), Comparison of modeled and empirical approaches for retrieving columnar water vapor from solar transmittance measurements in the 0.94- μ m region, *J. Geophys. Res.*, 101(D5), 9345–9358.
- Schmid, B., et al. (2001), Comparison of columnar water-vapor measurements from solar transmittance methods, *Appl. Opt.*, 40(12), 1886–1896.
- Schmid, B., et al. (2003), Column closure studies of lower tropospheric aerosol and water vapor during ACE-Asia using airborne sunphotometer, airborne in-situ and ship-based lidar measurements, *J. Geophys. Res.*, 108(D23), 8656, doi:10.1029/2002JD003361.
- Segal-Rosenheimer, M., P. B. Russell, J. M. Livingston, S. Ramachandran, J. Redemann, and B. A. Baum (2013), Retrieval of cirrus properties by Sun photometry: A new perspective on an old issue, *J. Geophys. Res. Atmos.*, 118, 4503–4520, doi:10.1002/jgrd.50185.
- Shinozuka, Y., et al. (2013), Hyperspectral aerosol optical depths from TCAP flights, *J. Geophys. Res. Atmos.*, 118, 12,180–12,194, doi:10.1002/2013JD020596.
- Shinozuka, Y., and J. Redemann (2011), Horizontal variability of aerosol optical depth observed during the ARCTAS airborne experiment, *Atmos. Chem. Phys.*, 11(16), 8489–8495.
- Tzortziou, M., J. R. Herman, A. Cede, and N. Abuhassan (2012), High precision, absolute total column ozone measurements from the Pandora spectrometer system: Comparisons with data from a Brewer double monochromator and Aura OMI, *J. Geophys. Res.*, 117, D16303, doi:10.1029/2012JD017814.
- Tzortziou, M., J. R. Herman, A. Cede, C. P. Loughner, N. Abuhassan, and S. Naik (2013), Spatial and temporal variability of ozone and nitrogen dioxide over a major urban estuarine ecosystem, *J. Atmos. Chem.*, doi:10.1007/s10874-013-9255-8.
- Vandaele, A. C., C. Hermans, P. C. Simon, M. Carleer, R. Colin, S. Fally, M. F. Me'rienne, A. Jenouvrier, and B. Coquart (1998), Measurements of the NO₂ absorption cross-section from 42000 cm⁻¹ to 10000 cm⁻¹ (238–1000 nm) at 220 K and 294 K, *J. Quant. Spectrosc. Radiat. Transfer*, 59(3–5), 171–184.
- Yokelson, R., et al. (2009), Emissions from biomass burning in the Yucatan, *Atmos. Chem. Phys. Discuss.*, 9(1), 767–835.
- Zelenyuk, A., J. Yang, E. Choi, and D. Imre (2009), SPLAT II: An aircraft compatible, ultra-sensitive, high precision instrument for in-situ characterization of the size and composition of fine and ultrafine particles, *Aerosol Sci. Technol.*, 43, 411–424.